RSC Advances

PAPER

View Article Online
View Journal | View Issue

Cite this: *RSC Adv.*, 2025, **15**, 30793

High-efficiency decontamination of pharmaceutical wastewater from γ-In_2Se_3/MoS_2/graphene composite driven by broad-spectrum absorption spanning ultraviolet to near-infrared irradiation

Xinyang Li,†[a] Zhigang Ruan,†[a] Ruimin Zhang,[a] Junchuan Wang*[ab] and Huayan Si *[ab]

Antibiotic contamination in water bodies poses a grave challenge to both environmental sustainability and human health. Among the emerging technologies for pharmaceutical pollutant decontamination, photocatalysis has garnered significant attention due to its superior efficiency. This study introduces a groundbreaking wide-spectral responsive γ-In_2Se_3/MoS_2/graphene composite system, fabricated through van der Waals interactions. To evaluate its photocatalytic activity, the system was tested against tetracycline (TC) degradation, demonstrating an impressive removal efficiency of 91% within 100 minutes. This performance far surpasses that of comparable systems γ-In_2Se_3 (60%) and γ-In_2Se_3/MoS_2 (79%). The superior efficiency is attributed to the synergistic effects arising from broad-spectrum absorption spanning ultraviolet to near-infrared wavelengths and optimized carrier separation kinetics, leading to a notable increase in photocatalytic activity. Furthermore, reactive oxygen species identification confirmed that surface-bound h^+ and $\cdot O_2^-$ are the primary intermediates governing the degradation process. The proposed degradation pathway for TC not only delineates the chemical transformation mechanisms but also underscores the significant reduction in wastewater toxicity post-catalytic treatment. Notably, the catalyst retains its excellent performance even after four consecutive cycles. These findings highlight the immense potential of this composite system for addressing antibiotic pollution in water resources and pave the way for future advancements in sustainable photocatalysis research.

Received 22nd July 2025
Accepted 21st August 2025

DOI: 10.1039/d5ra05282c

rsc.li/rsc-advances

1. Introduction

Antibiotics are pervasively administered for disease control in human healthcare and veterinary medicine, establishing them as significant contributors to persistent environmental micropollutants.[1,2] Tetracycline (TC) represents the second most prevalent class of broad-spectrum antibiotics globally and dominate agricultural applications due to their cost-effectiveness and potent antimicrobial properties.[3,4] However, limited absorption and metabolic breakdown in biological systems result in ingested TCs being excreted *via* urine or feces as parent compounds or bioactive derivatives.[4] This introduces substantial ecological burdens into aquatic ecosystems when discharged without adequate treatment. Furthermore, environmental dissemination of TCs accelerates the proliferation of antibiotic resistance genes among microbial populations, posing serious threats to public health.[3–5] Consequently, developing efficient strategies for TC elimination from wastewater streams has emerged as a critical environmental imperative. Among advanced oxidation processes, heterogeneous photocatalysis has emerged as a highly promising technique with the aid of solar energy for pharmaceutical pollutant degradation,[6–8] characterized by precluding secondary contamination high efficiency and sustainability.[9–11]

Among the various inorganic semiconductors, γ-indium selenide (γ-In_2Se_3) with band gap of 1.36–2.0 eV has stood out for its potential in organic pollutant degradation attributed to its low toxicity and environmental friendliness.[12–15] Furthermore, it is well recognized that it is difficult to impede the recombination of photogenerated electron–hole pairs and obtain optical absorption in a wide spectral range using a single semiconductor. In recent years, van der Waals (vdW) heterojunctions generated by assembling one monolayer on top of the other are found to be promising for tackling problems. In particular, molybdenum disulfide (MoS_2) monolayers of ultra-

[a]*School of Materials Science and Engineering, Shijiazhuang Tiedao University, Shijiazhuang 050043, China. E-mail: sihuayan@stdu.edu.cn; wangjunchuan@stdu.edu.cn; Tel: +86 311 8793 5411*

[b]*Hebei Provincial Key Laboratory of Traffic Engineering Materials, Shijiazhuang Tiedao University, Shijiazhuang 050043, China*

† X. Y. and Z. G. contributed equally to this work.

thin thickness show a narrow band gap and unique electrical properties.[16–19] By hanging bonds on the edge, the monolayer can facilitate high photocatalytic activity when used as a co-catalyst.

In recent years, considerable research efforts have been dedicated to exploring the intrinsic properties of In_2Se_3/MoS_2 composites. Zhang *et al.* conducted a theoretical investigation and demonstrated that the charge carrier mobility in this system is excellent due to its small effective mass and superior optical absorption capabilities across the infrared, visible, and ultraviolet spectra.[14] Furthermore, Jiang *et al.* reported significant advancements by employing In_2Se_3/MoS_2 heterojunctions as photoanodes, achieving a notably higher rate of O_2 evolution compared to pristine In_2Se_3.[20] This enhancement is attributed to the red shift of the system's light absorption spectrum from the visible to the infrared region and its ability to effectively suppress photogenerated carrier recombination. Additionally, the conductivity of catalysts has emerged as a critical factor in improving the performance of pharmaceutical pollutant degradation processes. Conductivity directly impacts the electronic properties of active sites and plays a crucial role in modulating electron transfer kinetics.[12,21] In this context, Dong *et al.* developed defective MoS_2/graphene heterostructures incorporating conductive 1T-phase MoS_2, which exhibited outstanding hydrogen evolution reaction (HER) performance and enhanced structural stability upon the introduction of graphene nanosheets.[21] Similarly, Zhang and coworkers reported a γ-In_2Se_3/α-In_2Se_3/graphene homoheterojunction that demonstrated a remarkable 3.25-fold increase in H_2 evolution rate compared to pristine In_2Se_3 nanoparticles, alongside excellent stability.[12] Given these promising results, the design of conductive heterojunction photocatalysts incorporating γ-In_2Se_3, MoS_2, and graphene show significant potential for enhancing photocatalytic performance. In such architectures, graphene contributes critical functions including exceptional charge carrier mobility, superior electrical conductivity, and an extensive surface area. However, a comprehensive experimental investigation and systematic analysis of the pharmaceutical pollutant degradation properties of γ-In_2Se_3/MoS_2/garphene heterojunctions remain absent in current literature. This study aims to address this gap by conducting detailed experiments and providing a thorough evaluation of their performance in pharmaceutical pollutant degradation processes.

Herein, γ-In_2Se_3/MoS_2/graphene composite was obtained *via* a simple ultrasonic method. The great pharmaceutical pollutant degradation activity of the γ-In_2Se_3/MoS_2/graphene composites is attributed to their broad-spectrum absorption spanning from ultraviolet to near-infrared wavelengths, coupled with stable interfacial interactions and efficient charge transfer dynamics between the γ-In_2Se_3, MoS_2, and graphene components. The γ-In_2Se_3/MoS_2 can facilitate charge carriers separation,[22–27] and graphene can accelerate the charge carriers migration, increase surface active sites, thereby boost the photocatalytic performance of γ-In_2Se_3/MoS_2. Finally, a possible transfer mechanism of photogenerated electron–hole over the γ-In_2Se_3/MoS_2/graphene composites is proposed.

2. Experimental section

2.1 Preparation of γ-In_2Se_3 nanosheets

An array of analytical-grade reagents was employed directly as received without additional purification. The γ-In_2Se_3 synthesis protocol was conducted under controlled conditions in a 100 mL three-necked round-bottom flask equipped with a condenser and maintained under an inert argon atmosphere. Following the pre-weighing of all precursor materials, the procedure proceeded as follows: (i) 0.45 mmol of selenium (Se), 0.3 mmol of indium chloride hexahydrate ($InCl_3 \cdot 4H_2O$), and 0.5 g of polyvinyl pyrrolidone (PVP) were sequentially introduced into the flask; (ii) the resulting mixture was stirred magnetically at room temperature to ensure complete dissolution; (iii) 0.1 mL of hydrazine hydrate ($N_2H_4 \cdot H_2O$) was carefully added dropwise to the solution; and (iv) the reaction mixture underwent rapid heating to 250 °C, where it was maintained for a dwell time of 30 minutes.

Upon completion of the reaction, the three-necked flask was permitted to cool rapidly to ambient temperature. The synthesized product, now in its crude form, was isolated *via* centrifugation and subsequently purified by sequential washing with anhydrous ethanol and deionized water. Finally, the obtained material was dried under vacuum at 60 °C for complete removal of residual solvent.

2.2 Synthesis of MoS_2 nanosheets

The synthesis of MoS_2 monomers was carried out *via* a hydrothermal procedure, employing well-defined precursor materials and optimized reaction conditions. Sodium molybdate dihydrate ($Na_2MoO_4 \cdot 2H_2O$) (48 mg) and thiourea ($(NH_2)_2CS$) (76 mg) were previously calcined and weighed with high precision to maintain a molar ratio of 1 : 5. These precursors were dissolved in 35 mL of deionized water, ensuring complete solubilization through thorough blending and magnetic stirring for 30 minutes. 10 mL of propionic acid was carefully incorporated into the solution to regulate the reaction pH. The resulting homogeneous mixture was then transferred into a 50 mL Teflon-lined stainless-steel autoclave, which was subjected to hydrothermal processing at 200 °C for an extended duration (24 h) in a convection oven. Upon completion of the reaction, the system was allowed to cool down naturally to room temperature. The black precipitate obtained post-reaction was isolated *via* centrifugation at 8000 rpm for 10 minutes. The recovered product was subjected to sequential purification by washing with deionized water and ethanol to eliminate residual impurities. Finally, the purified material was dried under vacuum conditions at 60 °C for a period of 12 hours to ensure complete removal of any remaining solvent residues.

2.3 Preparation of graphene samples

Graphene was firstly exfoliated from graphite by transition metal catalysts coordinated with electrochemistry method.[28] Then, 0.05 $g \cdot L^{-1}$ of graphene was obtained in the ethanol medium under ultrasonic dispersion treatment.

2.4 Preparation of γ-In_2Se_3/MoS_2/graphene composites

The pre-synthesized γ-In_2Se_3 nanosheets and MoS_2 nanosheets were initially mixed with triethylene glycol (TEG) solvent under ultrasonic treatment. Subsequently, reduced graphene oxide (graphene) sheets were incorporated into the suspension system. The resultant mixture underwent prolonged sonication at a power of 100 W and temperature of 30 °C for 30 minutes to ensure adequate dispersion and interfacial interaction. Following this step, the mixture was thoroughly purified by washing with ethanol and subjected to centrifugation at 8000 rpm for two consecutive cycles, thereby yielding the γ-In_2Se_3/MoS_2/graphene composites. A critical aspect of this procedure is that the graphene content in the final composite corresponds directly to its initial amount in the precursor solution. Therefore, the exact proportion of graphene can be accurately determined and quantified.

To conduct a systematic investigation, several composite samples with varying graphene contents (1%, 2%, 3%, 4%, and 5%) were prepared under identical reaction conditions. These samples were systematically designated as γ-In_2Se_3/MoS_2/graphene-*w*%, where *w* represents the respective weight percentages ($w = 1, 2, 3, 4, 5$). Furthermore, for comparative purposes, a γ-In_2Se_3/MoS_2 homojunction was fabricated using an analogous synthetic process without the addition of graphene. The mass ratio of γ-In_2Se_3 to MoS_2 was maintained at 40 : 1 for all samples.

3. Results and discussion

The γ-In_2Se_3/MoS_2/graphene composites were successfully synthesized *via* an ultrasonic method, as demonstrated by XRD and TEM characterizations. As shown in Fig. 1a, the XRD pattern of MoS_2 exhibits characteristic peaks at 14.37°, 33.51°, and 58.3°, corresponding to the (002), (100), and (110) planes of 2H-phase MoS_2 (JCPDS card no 37-1492).[29,30] Because of the characteristic peaks for 1T phase MoS_2 is close to 2H phase MoS_2 in the XRD pattern, to further confirm the phase structure, Raman spectroscopy was employed, revealing two distinct peaks at 381.0 cm^{-1} and 407.0 cm^{-1} in Fig. S1. These peaks correspond to the E12g and A1g vibrational modes of 2H-phase MoS_2,[31,32] with a peak position difference of 26 cm^{-1} indicating limited layer spacing for defective MoS_2.[29] This structural characteristic is advantageous for exposing catalytically active sites on the material surface.[32] The TEM images reveal the nanoplate morphology of MoS_2, as shown in Fig. 1b. The HRTEM analysis (Fig. 1c) confirms an interlayer distance of 0.63 nm, consistent with the (002) lattice spacing of MoS_2. For pure graphene, a broad diffraction peak at 26° is observed in Fig. 1d, indicative of its layered structure. The TEM image in Fig. 1e demonstrates that graphene forms transparent, sheet-like structures. Furthermore, the SAED pattern (Fig. 1f) displays a hexagonal arrangement corresponding to the (002) plane of graphene, confirming the formation of single-crystalline monolayer graphene sheets.[33] The XRD patterns in Fig. 1g establish that the primary structure of γ-In_2Se_3 corresponds to its hexagonal phase (JCPDS no 40-1407).[34] As shown in Fig. 1h, TEM reveals well-defined thin nanoplates. The lattice spacing of 0.36 nm observed in the HRTEM image of Fig. 1i matches the interplanar distance of γ-In_2Se_3. EDX elemental mapping (Fig. S2) further confirms the uniform distribution of In and Se elements with the atom ratio of In to Se 42.7 : 64.1, corresponding to the stoichiometric ratio of γ-In_2Se_3 consistent with its chemical formula. The SAED pattern (the insert of Fig. 1i) also supports the presence of a well-defined hexagonal lattice. For the γ-In_2Se_3/MoS_2/graphene composite, XRD analysis (Fig. 1j) shows no significant additional peaks corresponding to MoS_2 or graphene, suggesting that the amount of these components is below the detection limit. The TEM image in Fig. 1k reveals a highly dispersed distribution of nanoplates in which MoS_2 and graphene nanoplates maybe are inserted between and attached with γ-In_2Se_3 nanoplates. The HRTEM analysis in Fig. 1l further verifies that the obvious fringe spacing of 0.36 nm and 0.62 nm are ascribed to (110) and (002) facets of the γ-In_2Se_3 and MoS_2, respectively, while the non-lattice regions within the box belong to graphene. HRTEM analysis (Fig. 1l) of the interface region highlights the strong coupling effects between MoS_2, γ-In_2Se_3, and graphene components, facilitating efficient electron transfer and providing evidence for synergistic catalytic performance. Besides, the element mapping of In, Se, Mo, S and C in γ-In_2Se_3/MoS_2/graphene composite (Fig. S3) further confirm the successful introduction of the MoS_2 and graphene.

The chemical composition and oxidation states of the γ-In_2Se_3/MoS_2/graphene composite were systematically analyzed using XPS spectroscopy. As shown in Fig. 2a, the XPS spectrum reveals distinct peaks corresponding to In, Se, Mo, S, and C elements, confirming the successful integration of these components into the composite structure. For the In 3d and Se 3d spectra (Fig. 2b and c), a systematic shift toward higher binding energies was observed in the composite compared to pristine γ-In_2Se_3. Specifically, the In 3d peak shifted by approximately 0.7 eV, while the Se 3d peak exhibited a slight shift of about 0.4 eV (about 0.6 eV). These shifts can be attributed to the incorporation of sulfur atoms into the structure, which possess higher electronegativity than the other components in γ-In_2Se_3. This sulfur-induced electron redistribution leads to an increased electrostatic attraction between the outer-shell electrons and the nuclei of In and Se, resulting in their stronger binding.[20] The Mo 3d XPS spectrum (Fig. 2d) exhibited an additional peak near 229 eV, which can be attributed to the Se 3s contribution. This observation aligns with known XPS data,[35] demonstrating the interplay between different elements within the composite framework. In Fig. 2e, the Se $3p_{1/2}$ and Se $3p_{3/2}$ peaks (at binding energies of 162.3 eV and 159.6 eV, respectively) dominate the XPS spectrum of the γ-In_2Se_3/MoS_2/graphene composite, effectively obscuring the S 2p peaks. This indicates a preferential oxidation state for selenium in this structural arrangement.[32] Finally, as shown in Fig. 2f, the C 1s XPS spectrum of the graphene component reveals an increased intensity of the C=C bond. Furthermore, a slight redshift in binding energy is observed, consistent with enhanced chemical interactions at the interface between γ-In_2Se_3, MoS_2, and graphene. These observations collectively confirm the successful

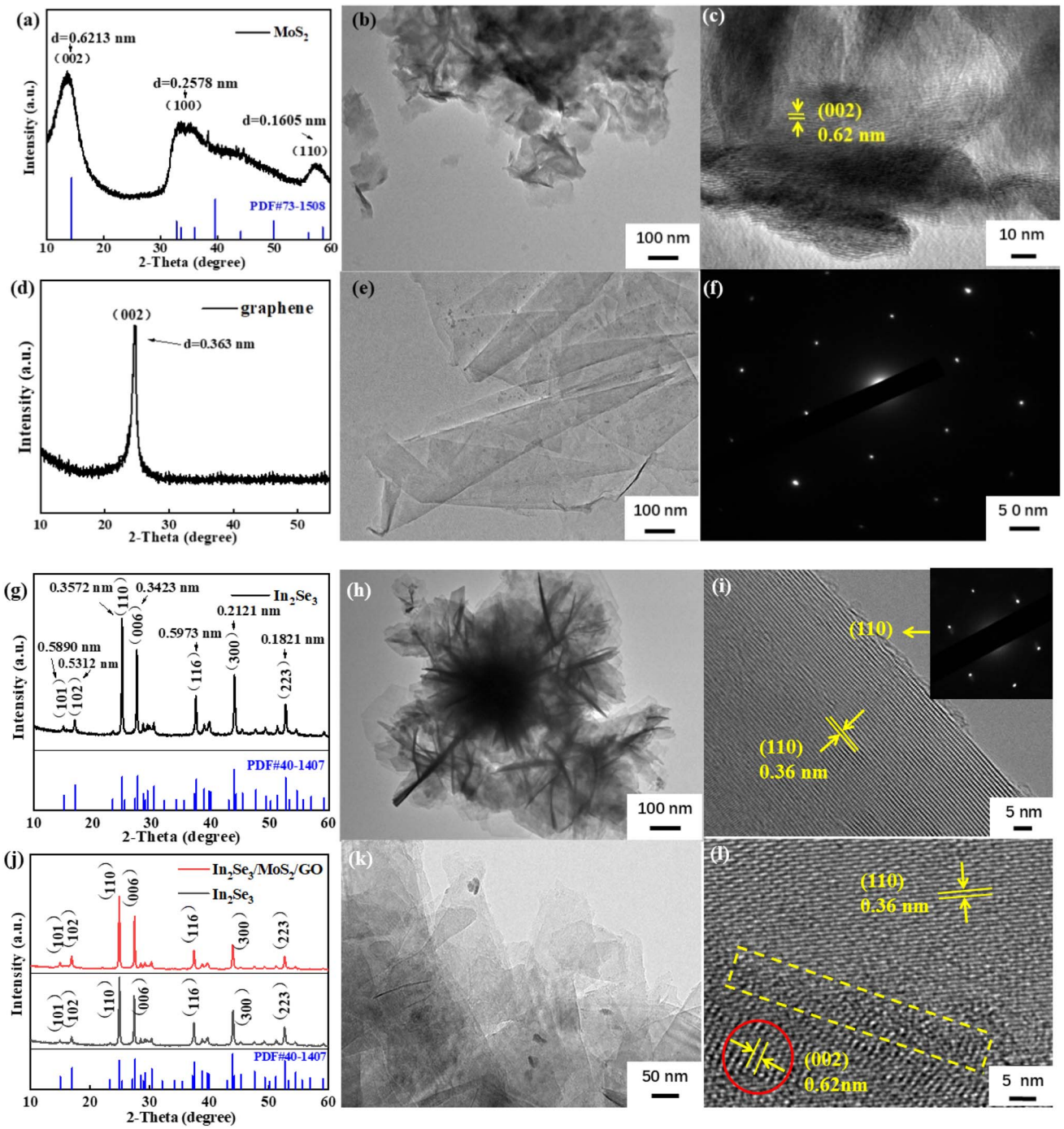

Fig. 1 (a) X-ray diffraction (XRD) pattern, (b) TEM and (c) HRTEM image of MoS_2 nanoplates; (d) XRD pattern, (e) TEM and (f) SEAD image of graphene; (g) XRD pattern of γ-In_2Se_3; (h) TEM and (i) HRTEM of γ-In_2Se_3, with SEAD pattern inserted in 2 (i); (j) XRD pattern, (k) TEM and (l) HRTEM of γ-In_2Se_3/MoS_2/graphene composite.

fabrication of the γ-In_2Se_3/MoS_2/graphene composite and highlight the intricate electronic correlations within its structure.[12]

The optical absorption properties of γ-In_2Se_3, MoS_2, graphene and the γ-In_2Se_3/MoS_2/graphene composite were systematically investigated to evaluate their light absorption characteristics. As shown in Fig. 3a, the γ-In_2Se_3/MoS_2/graphene composite exhibits significantly higher absorption intensity compared to pure γ-In_2Se_3 or pure MoS_2. The composite demonstrates a characteristic absorption edge and an apparent redshift in maximum-absorbance wavelength, extending from 700 nm to 800 nm. These results indicate that the composite enhances light absorption density and extends the photoresponse range into the infrared and UV regions attributed to the excellent UV-visible light absorption of graphene,[36,37] suggesting its potential as a high-performance

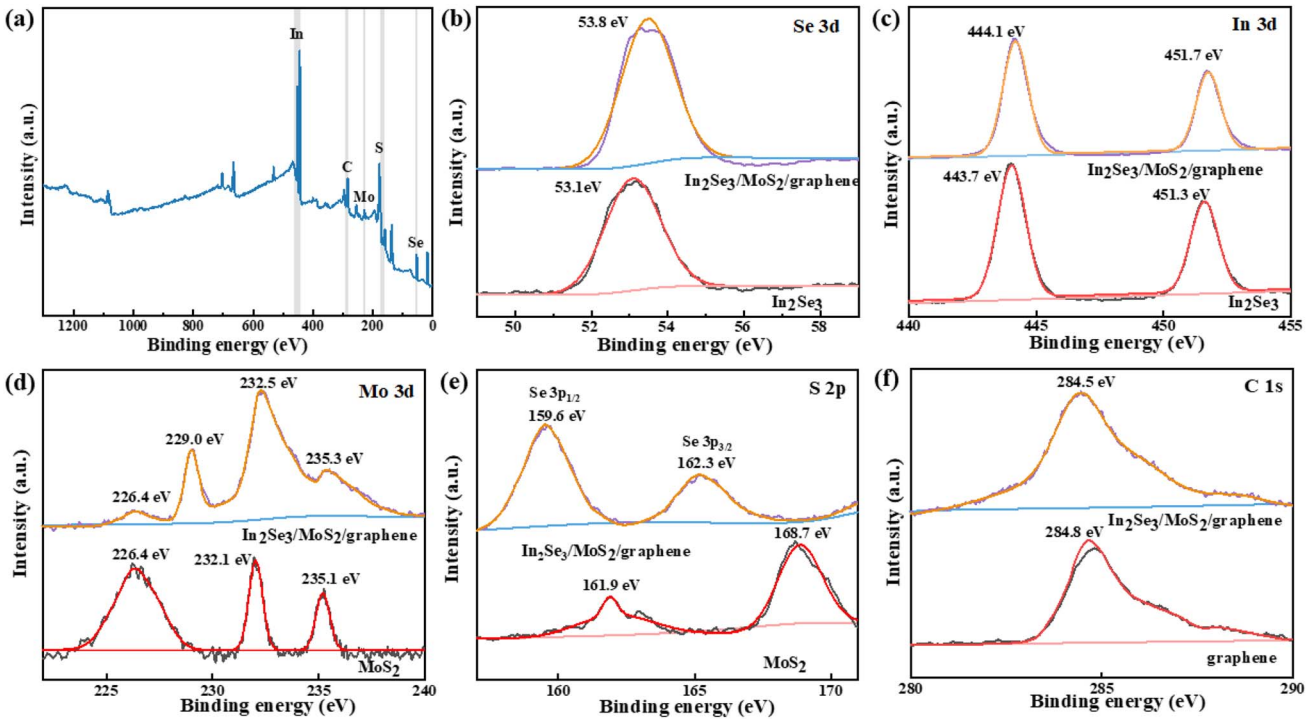

Fig. 2 High-resolution XPS spectra of γ-In_2Se_3/MoS_2/graphene composite: (a) survey spectrum, (b) Se 3d, (c) In 3d, (d) Mo 3d, (e) S 2p and (f) C 1s. Related XPS results of γ-In_2Se_3, MoS_2 and graphene are used as references.

photocatalyst.[14] Fig. 3b was derived using the Kubelka–Munk equation from the data presented in Fig. 3a.[38] The bandgap of γ-In_2Se_3 is determined to be 1.59 eV, while that of MoS_2 is calculated as 2.04 eV. These values provide valuable insights into the optical properties of the individual materials and their synergistic behavior within the composite structure.

Fig. 4a illustrates the transient photocurrent responses of the γ-In_2Se_3, γ-In_2Se_3/MoS_2, and γ-In_2Se_3/MoS_2/graphene composites under intermittent illumination. The photocurrent density, which directly reflects the efficiency of charge carrier separation and migration, increases significantly in the ternary composites, following the order: γ-In_2Se_3/MoS_2/graphene-4% > γ-In_2Se_3/MoS_2/graphene-5% > γ-In_2Se_3/MoS_2/graphene-3% > γ-In_2Se_3/MoS_2/graphene-2% > γ-In_2Se_3/MoS_2/graphene-1% > γ-In_2Se_3/MoS_2 > γ-In_2Se_3. This trend is not merely a statement of performance but is a direct consequence of the engineered heterojunction. The γ-In_2Se_3/MoS_2 interface forms a Type-I heterojunction, facilitating the transfer of photogenerated electrons from γ-In_2Se_3 to MoS_2 and holes in the opposite direction, thus initiating charge separation. The introduction of graphene, a highly conductive electron acceptor, further amplifies this process. Electrons from the conduction band of

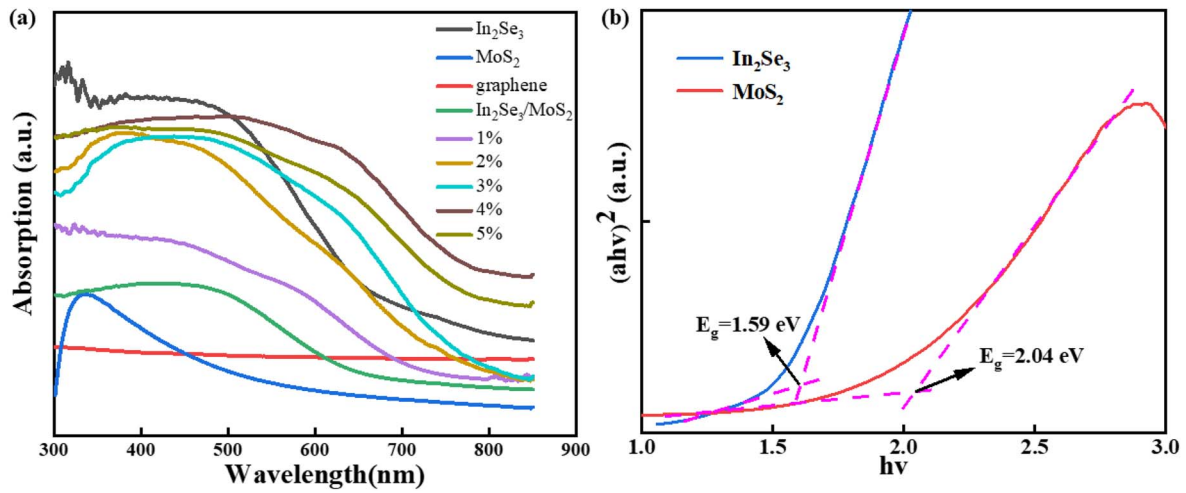

Fig. 3 (a) Absorbance spectra for γ-In_2Se_3, MoS_2, and the γ-In_2Se_3/MoS_2/graphene composites (1%, 2%, 3%, 4%, and 5% represents the amount of graphene in the γ-In_2Se_3/MoS_2/graphene composites, respectively); (b) bandgap curves of γ-In_2Se_3 and MoS_2.

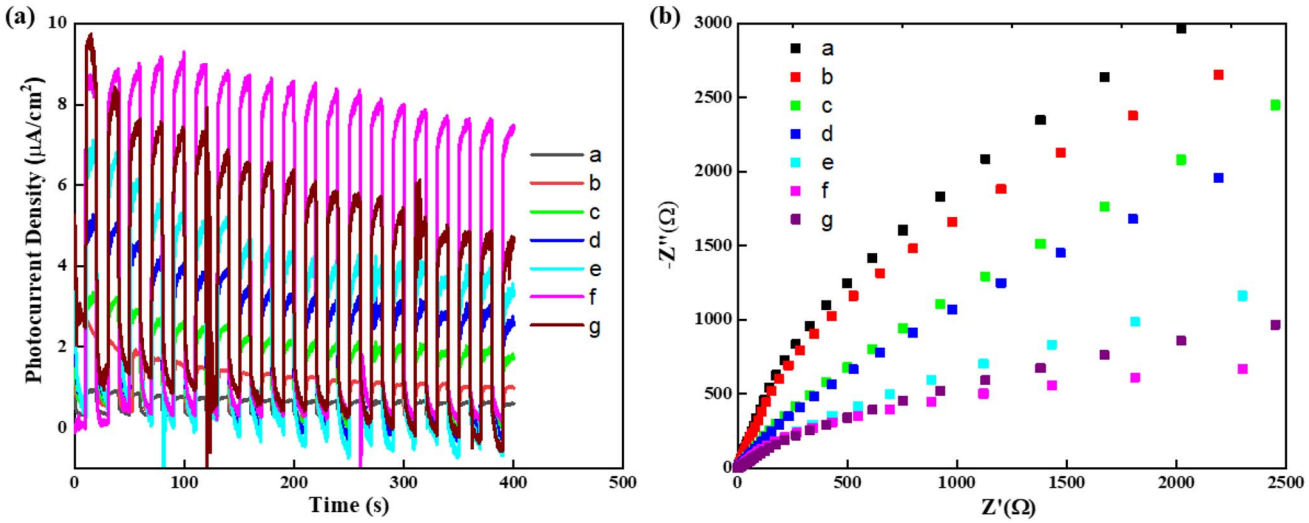

Fig. 4 (a) Transient photocurrent response curves and (b) EIS Nyquist plots of all the samples. (a) γ-In_2Se_3; (b) γ-In_2Se_3/MoS_2; (c–g) γ-In_2Se_3/MoS_2/graphene composites with the graphene amount of 1%, 2%, 3%, 4%, and 5%, respectively.)

MoS_2 (or directly from γ-In_2Se_3) are rapidly shuttled onto the graphene nanosheets.[39] This multi-step charge transfer pathway effectively spatially separates electrons (on graphene) from holes (remaining on γ-In_2Se_3), drastically reducing the probability of bulk recombination. The optimized 4% graphene loading represents the ideal balance between providing sufficient conductive pathways for electron extraction and avoiding the shielding of active sites or light absorption. The rapid decay of the photocurrent upon light cessation for all samples confirms the photogenerated nature of the current and the quick recombination dynamics once the excitation source is removed.

The electrochemical impedance spectroscopy (EIS) Nyquist plots under illumination (Fig. 4b) provide further electronic evidence for this mechanism. The diameter of the semicircular arc corresponds to the charge transfer resistance (R_{ct}) at the electrode–electrolyte interface. The significantly smallest arc radius observed for the γ-In_2Se_3/MoS_2/graphene-4% composite

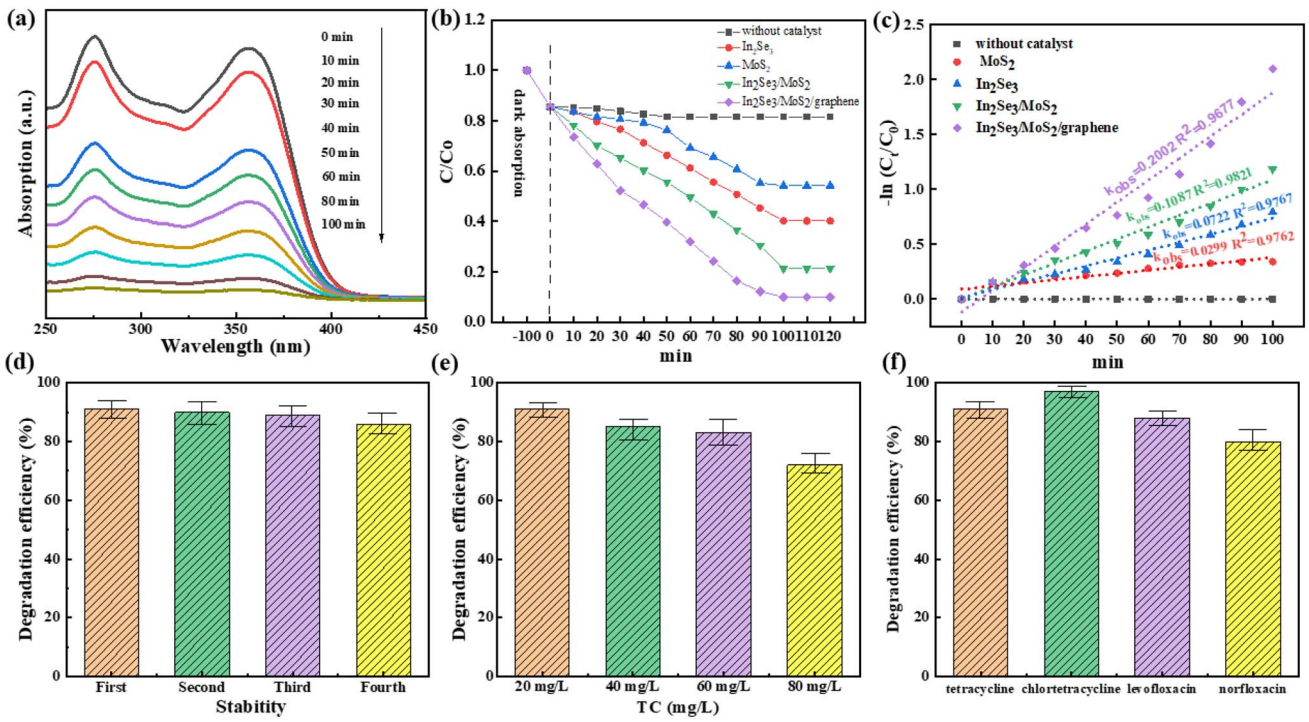

Fig. 5 (a) UV-vis absorption spectra of the TC solution photodegraded by γ-In_2Se_3/MoS_2/graphene composites; (b) TC removal under different conditions; (c) corresponding pseudo-first-order reaction kinetics curves; (d) stability of γ-In_2Se_3/MoS_2/graphene composites in photocatalysis of TC under visible light irradiation. (e) Effects of initial TC concentrations; (f) degradation efficiency of different antibiotic pollutants.

indicates the lowest R_{ct}. This is a quantifiable measure of the most efficient interfacial charge transfer and the smallest resistance to charge movement within the composite. This reduced impedance is a direct result of the synergistic effect within the ternary structure: graphene acts as a primary electron highway, drastically improving bulk electron conductivity, while the γ-In_2Se_3/MoS_2 heterojunction efficiently pumps electrons toward this highway. This integrated system minimizes charge accumulation and recombination losses, leading to the superior charge separation efficiency that correlates perfectly with the highest photocurrent generation.

The photocatalytic performance of the γ-In_2Se_3/MoS_2/graphene composite was assessed using various analytical techniques, including UV-Vis spectroscopy, kinetic modeling, stability tests, and mineralization studies. As demonstrated in Fig. 5a, the UV-Vis spectra confirmed the successful photodegradation of TC under visible light irradiation. As shown in Fig. 5b, the catalysts reached adsorption equilibrium in 100 min. Under visible light irradiation for the same period of time, the degradation efficiencies of MoS_2, γ-In_2Se_3, γ-In_2Se_3/MoS_2, and γ-In_2Se_3/MoS_2/graphene composite are 40%, 60%, 79%, and 91%, respectively. The photocatalytic performance of the γ-In_2Se_3/MoS_2/graphene composite for tetracycline (TC) degradation is comparable to previously reported benchmark materials (Table S1). The corresponding kinetics were analyzed using a $\ln(C_0/C_t)$ *vs.* time plot, which exhibits a near-linear relationship indicative of first-order kinetics. As shown in Fig. 5c, the rate constants observed for MoS_2, γ-In_2Se_3, γ-In_2Se_3/MoS_2 and the hybrid composite are 0.0299, 0.0722 min^{-1}, 0.1087 min^{-1} and 0.2022 min^{-1}, respectively. This represents a significant enhancement in catalytic activity, with the hybrid composite demonstrating approximately 2.8-fold faster performance compared to stand-alone γ-In_2Se_3.

The stability and reproducibility of the photocatalyst were assessed through four consecutive degradation cycles, as illustrated in Fig. 5d. After each cycle, the catalyst was filtered, washed, dried, and reutilized without any pretreatment. The observed TC degradation efficiencies remained consistent across all cycles (91% ± 2%, 91% ± 3%, 90% ± 3%, and 88% ± 2%), highlighting excellent stability. Supporting evidence for this structural integrity was obtained from XPS, XRD, and SEM analyses of the composite before and after four reaction runs (Fig. S4). These analyses revealed no significant changes in oxidation state, crystal structure, or surface morphology, confirming that the photocatalyst maintains its chemical stability over repeated use. The slight attenuation in photocatalytic

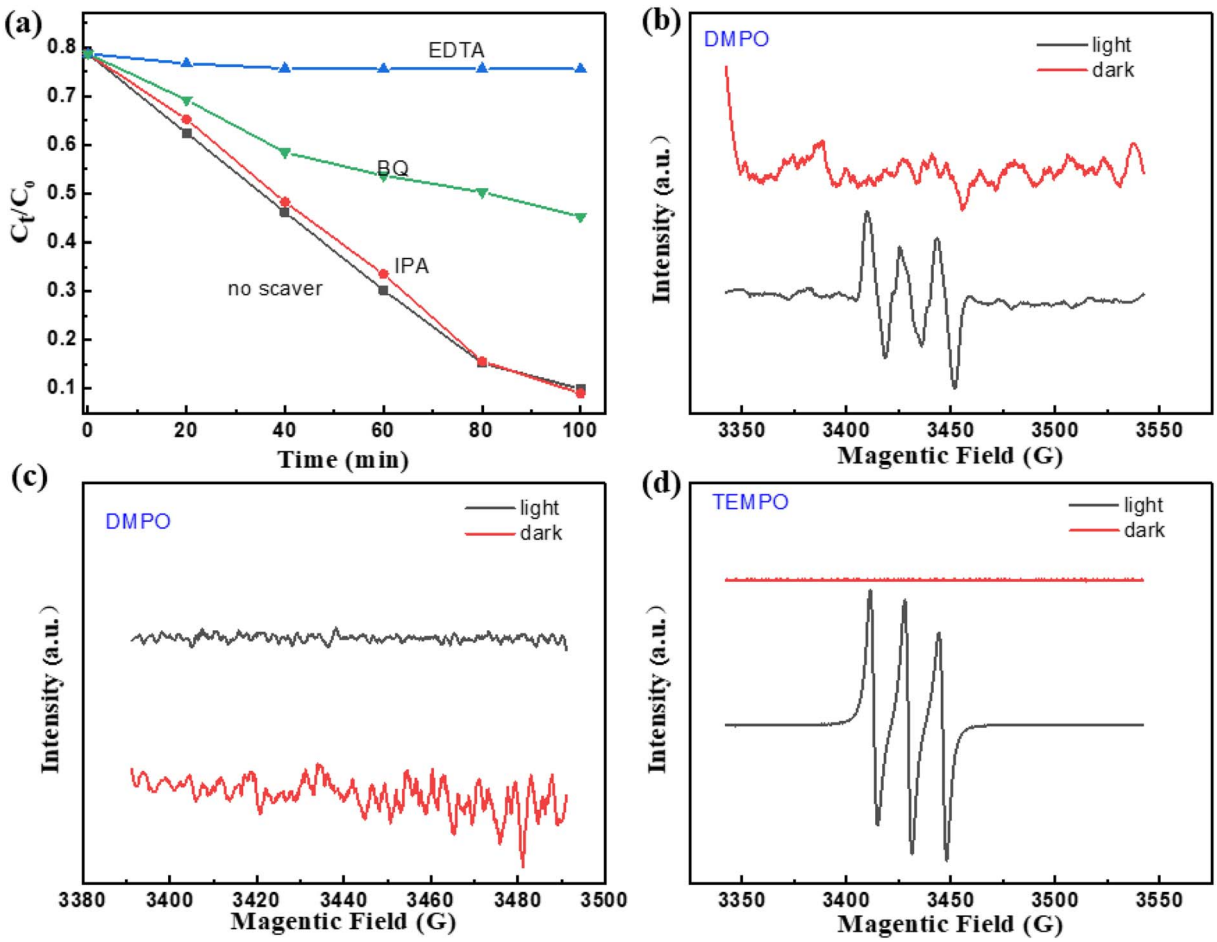

Fig. 6 (a) Effect of quenching reagents on TC degradation; (b) DMPO-·O_2^- and (c) DMPO-·OH with irradiation for 30 s in methanol and aqueous dispersion, respectively. (d) TEMPO-h^+ with irradiation for 30 s in methanol.

efficiency observed over four consecutive cycles could be primarily ascribed to the inevitable partial loss of catalyst mass during the recovery process or the strong adsorption of stable intermediate byproducts generated during TC degradation onto the active sites of the catalyst.

The influence of initial substrate concentration on photodegradation efficiency was evaluated by varying the TC concentration from 0.02 to 0.1 g L^{-1} (Fig. 5e). A clear correlation between increasing concentration and reduced degradation efficiency was observed. Notably, at an initial TC concentration of 0.08 g L^{-1}, the degradation efficiency dropped significantly to only 70% ± 3%, suggesting that substrate concentration plays a critical role in determining reaction kinetics.

In addition to its performance against TC, the γ-In_2Se_3/MoS_2/graphene composite demonstrated excellent photocatalytic activity towards other waterborne antibiotic pollutants. The chemical structures of the chosen antibiotics are demonstrated in Fig. S5. As depicted in Fig. 5f, we tested its efficiency on chlorotetracycline (CTC), levofloxacin (LEV), and norfloxacin (NOR). The respective degradation efficiencies achieved were 98.6% ± 2%, 90.4% ± 2%, and 88.4% ± 2%, which underscores the broad applicability of this photocatalyst for diverse antibiotic contaminants. To further evaluate the mineralization efficiency, we monitored total organic carbon (TOC) removal during the photodegradation process (Fig. S6). The TOC removal efficiencies attained for TC, LEV, NOR, and CTC were 62.7%, 65.0%, 69.4%, and 42.5%, respectively. These results demonstrate that the γ-In_2Se_3/MoS_2/graphene composite not only effectively degrades antibiotic pollutants but also achieves substantial mineralization, thereby offering a promising solution for environmental remediation.

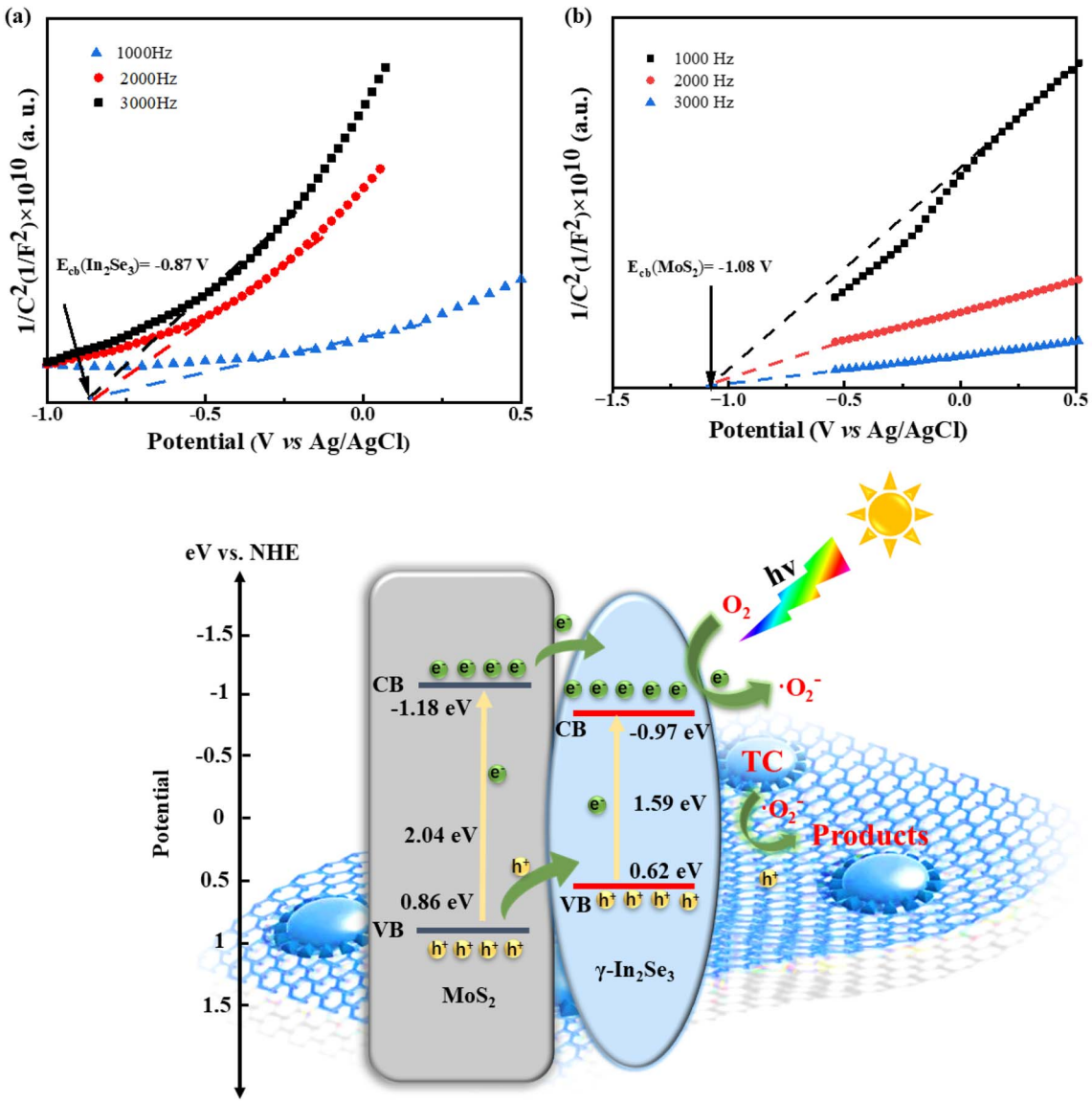

Fig. 7 Mott–schottky curves of (a) γ-In_2Se_3 and (b) MoS_2. (c) Proposed mechanism of charge transfer for the photocatalytic degradation of TC by the γ-In_2Se_3/MoS_2/graphene composite.

These findings collectively suggest that the γ-In_2Se_3/MoS_2/graphene hybrid system exhibits superior photocatalytic performance, excellent stability, and wide applicability towards diverse antibiotic contaminants, making it a highly prospective candidate for water treatment applications.

The photocatalytic reaction mechanism of the γ-In_2Se_3/MoS_2/graphene composite system was investigated by analyzing the involvement of free radicals through experiments with radical scavengers in TC-containing solutions. As shown in Fig. 6a, the effects of different radical species were evaluated using specific scavenger agents. EDTA was used to capture h^+ ions; upon its addition, the photocatalytic degradation efficiency of the composite system was significantly reduced, indicating that h^+ plays a critical role in the degradation process of TC solutions. Benzyl quinoline (BQ) was employed as a scavenger for $\cdot O_2^-$ radicals, and its presence exhibited some inhibitory effects on the photocatalytic degradation efficiency. However, isopropyl alcohol (IPA), used to scavenge ·OH radicals, showed no significant impact on the photocatalytic performance of the composite system, suggesting that ·OH radicals are not dominant species in this mechanism. Based on these results, H^+ and $\cdot O_2^-$ were identified as the primary active species involved in the photocatalytic degradation of TC by the γ-In_2Se_3/MoS_2/graphene system. This conclusion was further supported by electron paramagnetic resonance (EPR) studies, which provided additional evidence for the involvement of these radicals. The EPR experiments were performed separately in methanol and water media under visible light irradiation. As demonstrated in Fig. 6b, the presence of characteristic DMPO-$\cdot O_2^-$ adduct peaks confirms the involvement of $\cdot O_2^-$ radicals during the photocatalytic process. In contrast, no DMPO-··OH signals were observed in Fig. 6c, indicating that ·OH radicals play a negligible role in this system. Furthermore, TEMPO-h^+ spectra in Fig. 6d revealed the distinct triplet signal characteristic of h^+ species, confirming their presence in the γ-In_2Se_3/MoS_2/graphene composite system. These observations collectively confirm that the dominant active species responsible for TC degradation are h^+ and $\cdot O_2^-$ radicals under visible light irradiation.

To analyze the photogenerated carrier separation mechanism, we investigated the energy band structures of the single-component materials (γ-In_2Se_3 and MoS_2). The Mott–Schottky (MS) curves for γ-In_2Se_3 and MoS_2 at different frequencies (1000, 2000, and 3000 Hz) revealed their n-type characteristics, with flat band potentials of −0.87 V and −1.08 V, respectively (Fig. 7a and b)). For n-type semiconductors, the conduction band (CB) potential is typically 0.1–0.2 V more negative than the flat band potential,[40] The small discrepancy in this case is negligible and does not significantly impact the overall mechanism. The band energy mechanism diagram provided in Fig. 7c illustrates the electronic interaction between γ-In_2Se_3 and MoS_2 under visible light illumination. Upon excitation, photogenerated electrons in the CB of MoS_2 are transferred to the CB of γ-In_2Se_3, while holes in the valence band (VB) of MoS_2 migrate to the VB of γ-In_2Se_3. This efficient electron and hole transfer process is facilitated by the graphene component, which accelerates electron transfer kinetics, ensuring excellent conductivity and structural stability of the composite catalyst. The transferred electrons and holes migrate across the graphene layer to the semiconductor surface, where they react with dissolved oxygen to generate superoxide radicals ($\cdot O_2^-$), which possess strong oxidizing properties. These radicals facilitate the rapid degradation of TC molecules into intermediate products and other byproducts.

The degradation of TC was investigated using High-performance liquid chromatography-mass spectrometry (HPLC-MS), which identified intermediates formed during the process (Fig. S7). Three primary degradation pathways were observed and characterized as follows in Fig. 8. For pathway I, the initial step involves demethylation of TC, leading to the formation of intermediate A with a mass-to-charge ratio (m/z) of 431. Subsequent dealcoholization results in intermediate D (m/z = 413), which undergoes a series of ring-opening reactions. These reactions ultimately produce intermediates G (m/z = 278)

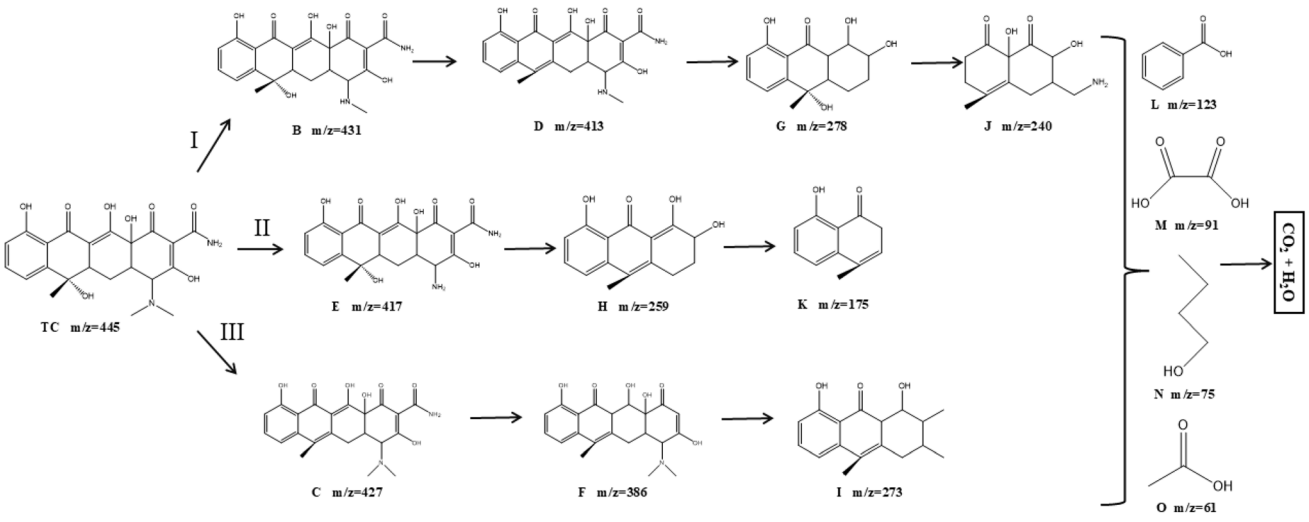

Fig. 8 Proposed TC degradation pathway in the γ-In_2Se_3/MoS_2/graphene composite system.

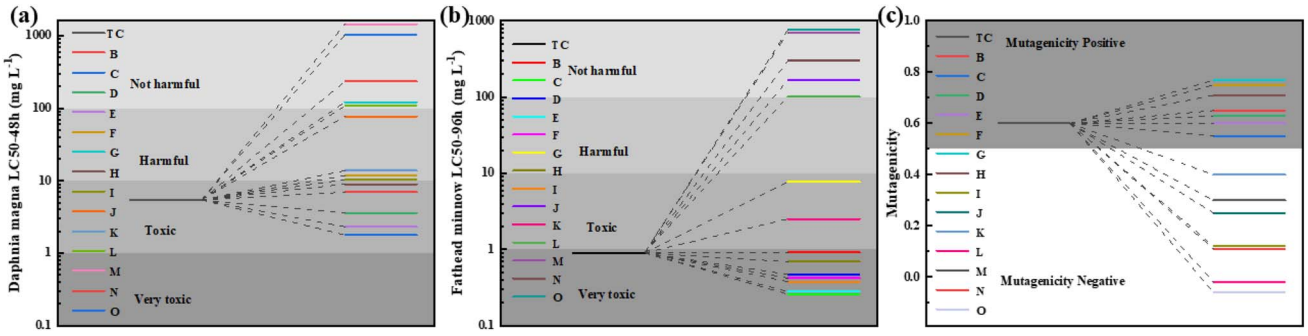

Fig. 9 (a) Daphnia magna LC50-48h of TC and degradation intermediates; (b) fathead minnow LC50-96h of TC and degradation intermediates; (c) mutagenicity of TC and degradation intermediates.

and J ($m/z = 240$). For pathway II, Intermediate E ($m/z = 417$) is generated through the demethylation of the dimethylamino group in TC, facilitated by reactive species. Hydroxylation of E yields intermediate H ($m/z = 259$), which undergoes dehydration, deamination, and further ring-opening reactions to form K ($m/z = 175$). In terms of pathway III, dehydration of TC results in intermediate C ($m/z = 427$).[41] This compound subsequently loses its amide and methyl groups, forming intermediate F ($m/z = 386$). Deamination and additional ring-opening reactions produce I ($m/z = 273$), under the continuous action of active species. In all pathways, the small molecule intermediates ultimately undergo complete mineralization into inorganic substances such as carbon dioxide and water.[42]

The toxicity of TC (TC) pollutants and their potential degradation intermediates was evaluated using the Toxicity Estimation Software Tool (TEST).[43] As demonstrated in Fig. 9a, the Daphnia magna LC50-48h value for TC was determined to be 5.44 mg L^{-1}, highlighting its inherent toxicity. Notably, except for intermediates C, D, and E, the LC50-48h values of other intermediates for Daphnia magna were observed to be higher than that of TC, suggesting a substantial reduction in toxicity post-degradation. Furthermore, as shown in Fig. 9b, while some intermediates exhibited Fathead minnow LC50-96h values exceeding the TC benchmark of 0.90 mg L^{-1}, the final degradation product displayed a non-toxic profile with an LC50-96h value. The mutagenicity predictions presented in Fig. 9c reveal that certain intermediates retained mutagenic potential; however, the final product exhibited diminished mutagenicity, reaching negative levels. These findings underscore the effectiveness of the γ-In_2Se_3/MoS_2/graphene composite catalyst in degrading TC and diminishing its overall toxicity. It is imperative to recognize that toxic intermediates are generated during the degradation process. Consequently, achieving a high degree of oxidation or mineralization is crucial to ensure the safety of treated water, thereby mitigating potential ecological risks.

4. Conclusion

In summary, an innovative γ-In_2Se_3/MoS_2/graphene composite was successfully synthesized *via* a facile ultrasonic-assisted method. This broad-spectrum-responsive photocatalyst demonstrated outstanding degradation performance toward various antibiotics, achieving efficiencies of 91.0%, 98.6%, 90.4%, and 88.4% for TC, CTC, LEV, and NOR, respectively. Mechanism studies revealed that the significantly enhanced activity originates from the type-I heterojunction between γ-In_2Se_3 and MoS_2, which facilitates efficient charge separation, coupled with the superior electron-transfer capability of graphene that further suppresses carrier recombination. A degradation pathway for TC was proposed alongside toxicity assessment of intermediates. This work provides a highly efficient and environmentally sustainable photocatalytic system with promising potential for antibiotic remediation in wastewater.

Author contributions

Xinyang Li and Zhigang Ruan: methodology, investigation, writing original draft, and Xinyang Li and Zhigang Ruan contributed equally to this work. Ruimin Zhang: validation, methodology, investigation. Junchuan Wang: methodology, investigation, writing–review&editing. Huayan Si: methodology, investigation, writing–review&editing, funding acquisition, conceptualization.

Conflicts of interest

The authors declare that they have no known competing financial interests or personal relationships that could have appeared to influence the work reported in this paper.

Data availability

The authors confirm that the data supporting the findings of this study area vailable within the article. Additional Raman, EDS, XPS analysis, HPLC-MS result and so on. Supplementary data to this article can be found online. See DOI: **https://doi.org/10.1039/d5ra05282c**.

Acknowledgements

This present work was financially supported by Natural Science Foundation of Hebei Education Department (ZD2021095), College Student Innovation and Entrepreneurship Program and Hebei Key Discipline Construction Project.

References

1 Y. F. Ji, Y. Y. Shi, W. Dong, X. Wen, M. D. Jiang and J. H. Lu, *Chem. Eng. J.*, 2016, **298**, 225–233.
2 J. H. Zhou, X. S. Li, J. Yuan and Z. W. Wang, *Chem. Eng. J.*, 2022, **441**, 136061.
3 H. Fang, H. F. Wang, L. Cai and Y. L. Yu, *Environ. Sci. Technol.*, 2015, **49**, 1095–1104.
4 J. B. Wang, D. Zhi, H. Zhou, X. W. He and D. Y. Zhang, *Water Res.*, 2018, **137**, 324–334.
5 J. Zuber, K. McJunkin, C. Fellmann, L. E. Dow, M. J. Taylor, G. J. Hannon and S. W. Lowe, *Nat. Biotechnol.*, 2011, **29**, 79–83.
6 A. Q. Wang, Z. K. Zheng, H. Wang, Y. W. Chen, C. H. Luo, D. J. Liang, B. W. Hu, R. L. Qiu and K. Yan, *Appl. Catal. B Environ.*, 2020, **277**, 119171.
7 Y. Zhang, J. B. Zhou, J. H. Chen, X. Q. Feng and W. Q. Cai, *J. Hazard. Mater.*, 2020, **392**, 122315.
8 B. Weng, M. Zhang, Y. Z. Lin, J. C. Yang, J. Q. Lv, N. Han, J. F. Xie, H. P. Jia, B. L. Su, M. Roeffaers, J. Hofkens, Y. F. Zhu, S. B. Wang, W. Y. Choi and Y. M. Zheng, *Nat. Rev. Clean Technol.*, 2025, **1**, 201–215.
9 C. R. Chen, H. Y. Zeng, M. Y. Yi, G. F. Xiao, R. L. Zhu, X. J. Cao, S. G. Shen and J. W. Peng, *Ecotox. Environ. Safe.*, 2019, **172**, 423–431.
10 C. Y. Zhou, C. Lai, P. Xu, G. M. Zeng, D. L. Huang, Z. H. Li, C. Zhang, M. Cheng, L. Hu, J. Wan, F. Chen, W. P. Xiong and R. Deng, *ACS Sustainable Chem. Eng.*, 2018, **6**, 6941–6949.
11 Z. Xie, Y. Feng, F. Wang, D. Chen, Q. Zhang, Y. Zeng, W. Lv and G. Liu, *Appl. Catal. B Environ.*, 2018, **229**, 96–104.
12 Q. Q. Zhang, R. M. Wang, X. Xie, C. N. Tang, X. Y. Hu, J. Fan and E. Z. Liu, *Int. J. Hydrogen Energy*, 2020, **45**, 33370–33380.
13 J. O. Island, S. I. Blanter, M. Buscema, H. S. v. d. Zant and A. Castellanos-Gomez, *Nano Lett.*, 2015, **15**, 7853–7858.
14 J. R. Zhang, X. Z. Deng, B. Gao, L. Chen, C. T. Au, K. L. Li, S. F. Yin and M. Q. Cai, *Catal. Sci. Technol.*, 2019, **9**, 4659.
15 X. F. Wei, H. Feng, L. W. Li, J. B. Gong, K. Jiang, S. L. Xue and P. K. Chu, *Appl. Catal. B Environ.*, 2020, **260**, 18218.
16 J. R. Zhang, Y. Q. Zhao, L. Chen, S. F. Yin and M. Q. Cai, *Appl. Surf. Sci.*, 2019, **469**, 27–33.
17 Z. F. Zhang, Q. K. Qian, B. K. Li and K. J. Chen, *ACS Appl. Mater. Interfaces*, 2018, **10**, 17419–17426.
18 B. Liu, Y. Q. Zhao, Z. L. Yu, L. Z. Wang and M. Q. Cai, *J. Colloid Interface Sci.*, 2018, **513**, 677–683.
19 H. W. Tian, M. Liu and W. T. Zheng, *Appl. Catal. B Environ.*, 2018, **225**, 468–476.
20 Y. Jiang, Q. Wang, L. Han, X. Y. Zhang, Z. Z. Wu, Y. Q. Lai, D. Z. Wang and F. Y. Liu, *Chem. Eng. J.*, 2019, **358**, 752–758.
21 W. M. Dong, H. Liu, X. X. Liu, H. Y. Wang, X. R. Li and L. J. Tian, *Int. J. Hydrogen Energy*, 2021, **46**, 9360–9370.
22 S. W. C. Chien, D. Q. Ng, D. Kumar, S. M. Lam and Z. H. Jaffari, *J. Phys. Chem. Solids*, 2022, **160**, 110342.
23 S. M. Lam, M. K. Choong, J. C. Sin, H. H. Zeng, L. L. Huang, L. Hua, H. X. Li, Z. H. Jaffari and K. H. Cho, *J. Environ. Chem. Eng.*, 2022, **10**, 108284.
24 S. M. Lam, S. M. Wong, J. C. Sin, H. H. Zeng, H. X. Li, L. L. Huang, H. Lin, A. R. Mohamed, J. W. Lim and Z. Z. Qin, *Environ. Res.*, 2024, **261**, 119718.
25 S. M. Lam, Z. J. Yong, J. C. Sin, A. R. Mohamed, H. H. Zeng, H. X. Li, H. Lin, L. L. Huang, H. T. Huang, L. W. Xu, J. W. Lim and K. Dong, *Appl. Surf. Sci.*, 2025, **691**, 162702.
26 Z. J. Yong, S. M. Lam, J. C. Sin, H. H. Zeng, A. R. Mohamed and Z. H. Jaffari, *Inorg. Chem. Commun.*, 2022, **143**, 109826.
27 S. M. Lam, J. C. Sin, H. H. Zeng, H. X. Li, H. Lin, L. L. Huang, J. W. Lim and K. Dong, *Sep. Purif. Technol.*, 2024, **329**, 125249.
28 H. X. Kang, K. X. Zhang, X. Y. Tian, Z. G. Ruan, Z. X. Xiao, Y. X. Jin, H. Y. Si and Y. T. Li, *Appl. Catal. O*, 2024, **194**, 206978.
29 X. Gao, J. Qi, S. Wan, W. Zhang, Q. Wang and R. Cao, *Small*, 2018, **14**, e1803361.
30 S. Jayabal, G. Saranya, Y. Liu, D. Geng and X. Meng, *Sustain. Energy Fuels*, 2019, **3**, 2100–2109.
31 H. Liu, X. Chen, L. Deng, X. Su, K. Guo and Z. Zhu, *Electrochim. Acta*, 2016, **206**, 184–191.
32 L. B. Huang, L. Zhao, Y. Zhang, C. Y. Y, Q. H. Zhang, H. Luo, X. Zhang, T. Tang, L. Gu and J. S. Hu, *Adv. Energy Mater.*, 2018, **8**, 1800734.
33 K. Parvez, R. J. Li and e. a. S. R. Punired, *ACS Nano*, 2013, **7**, 3598.
34 S. Yang, C. Y. Xu, L. Yang, S. P. Hu and L. Zhen, *RSC Adv.*, 2016, **6**, 106671–106675.
35 D. W. Langer and C. J. Vesely, *Phys. Rev. B:Condens. Matter Mater. Phys.*, 1970, **2**, 4885.
36 S. Gayathri, P. Jayabal, M. Kottaisamy and V. Ramakrishnan, *AIP Adv.*, 2014, **4**, 027116.
37 H. Lin, B. C. P. Sturmberg, K. T. Lin, Y. Y. Yang, X. R. Zheng, T. K. Chong, C. M. D. Sterke and B. H. Jia, *Nat. Photonics*, 2019, **13**, 270–276.
38 H. W. Huang, J. W. Zhao, H. L. Guo, B. Weng, H. W. Zhang, R. A. Saha, M. L. Zhang, F. L. Lai, Y. F. Zhou, R. Z. Juan, P. C. Chen, S. B. Wang, J. A. Steele, F. L. Zhong, T. X. Liu, J. Hofkens, Y. M. Zheng, J. L. Long and M. B. J. Roeffaers, *Adv. Mater.*, 2024, **36**, 2313209.
39 Y. Mu, W. Zhang, G. Dong, K. Su, M. Zhang and T. Lu, *Small*, 2020, **16**, 2002140.
40 S. Zhang, L. Chen, J. Shen, Z. Li, Z. Wu, W. Feng, K. Xu, D. Xu, X. Chen and S. Zhang, *Ceram. Int.*, 2019, **45**, 18065–18072.
41 J. Y. Xin, Y. Liu, L. Y. Niu, F. Zhang, X. H. Li, C. L. Shao, X. W. Li and Y. C. Liu, *Chem. Eng. J.*, 2022, **445**, 136616.
42 R. Y. Chen, H. Y. Zhang, Y. M. Dong and H. F. Shi, *J. Mater. Sci. Technol.*, 2024, **170**, 11–24.
43 Y. T. Ai, S. A. C. Carabineiro, X. Q. Xiong, H. Y. Zhu, Q. Wang, B. Weng and M. Q. Yang, *Chin. J. Catal.*, 2025, **75**, 147–163.